Rapid Communications

Magnetotransport properties of the correlated topological nodal-line semimetal YbCdGe

Antu Laha,[1] Sudip Malick,[1] Ratnadwip Singha,[2] Prabhat Mandal,[2] P. Rambabu,[3,4] V. Kanchana,[3] and Z. Hossain[1,*]

[1]*Department of Physics, Indian Institute of Technology, Kanpur 208016, India*

[2]*Saha Institute of Nuclear Physics, HBNI, 1/AF Bidhannagar, Calcutta 700 064, India*

[3]*Department of Physics, Indian Institute of Technology Hyderabad, Kandi, Medak 502 285, Telengana, India*

[4]*Department of Pure and Applied Physics, Guru Ghasidas Vishwavidyalaya, Koni, Bilaspur 495009, India*

(Received 31 January 2019; revised manuscript received 17 May 2019; published 4 June 2019)

Realization of strong correlation effect in topological materials is very rare due to lack of ideal systems. In this Rapid Communication, we present the magnetotransport properties of a correlated nodal-line semimetal YbCdGe. A valence fluctuating state has been observed through magnetic susceptibility and specific heat data. This compound shows an extremely large, nonsaturating transverse magnetoresistance (1.14×10^3% at 3 K and 12 T). The cusplike magnetoconductivity at low magnetic field indicates the presence of weak antilocalization. The origin of this phenomenon is further supported from the direction dependent transport measurements. Magnetic field-induced metal-semiconductor-like crossover and a plateau in resistivity are observed at low temperature which are common features of topological semimetals. Hall measurement and electronic band-structure calculation suggest that YbCdGe is a topological nodal-line semimetal with higher carrier (hole) density than a typical Dirac/Weyl semimetal.

DOI: 10.1103/PhysRevB.99.241102

While symmetry protected nontrivial topological state is one of the vastly studied fields of condensed matter physics in recent times, the effect of strong electronic correlation in such a state remains largely unexplored. There are only a few topological materials, which exhibit strongly correlated phenomenon such as valence fluctuation, heavy fermion behavior, etc. [1–3]. Discovery of the topological Kondo insulating state in intermediate valence compound SmB_6 [4] opens up a new area of interest for topological phases in the presence of strong correlation. Subsequently, a topological insulator (TI) state has been observed in Yb-based mixed valence borides such as YbB_6 and YbB_{12} [5,6]. Moreover, the Weyl fermionic state has been probed in canonical heavy fermion semimetals YbPtBi [3] and $CeRu_4Sn_6$ [7]. Recently, strong electron-electron correlation effect is also predicted theoretically for the topological nodal-line semimetal ZrSiS [8]. Furthermore, magnetic field induced unconventional mass enhancement of charge carriers around the Dirac nodal loop is observed experimentally in this material [9], which is reminiscent of quasiparticle mass enhancement at magnetic field tuned quantum critical point in correlated systems such as $YbRh_2Si_2$ [10] and $CeCoIn_5$ [11]. Therefore, it is worthwhile to investigate the interplay between topological states and strongly correlated phenomenon, which may lead to novel quantum phases of matter.

CaCdGe is a noncorrelated compound with multiple Fermi pockets near the Fermi level and hosts topological nodal-line state in its electronic band structure [12]. Replacing calcium with ytterbium keeps the crystal structure unaltered but introduces strong electronic correlation in the system. In the present work, we have studied the magnetotransport properties of single crystalline YbCdGe along with its electronic band structure. A valence fluctuating state is observed, which is a signature of strongly correlated electrons. Similar to several topological semimetals (TSMs), this material also shows a large and nonsaturating magnetoresistance (MR) as well as magnetic field induced metal-semiconductor-like crossover and resistivity plateau. We have also observed weak antilocalization effect (WAL) in the magnetotransport properties. Furthermore, low carrier density is found from Hall measurements. Band-structure calculations shows that YbCdGe is a topological nodal-line semimetal.

Single crystals of YbCdGe were grown using cadmium flux. Yb ingot (99.99%, Alfa Aesar), Cd shot (99.99%, Alfa Aesar) and Ge pieces (99.999%, Alfa Aesar) were taken in 1:47:1 ratio in an alumina crucible, which was then sealed with argon inside a quartz ampoule. The ampoule was heated to 1000 °C and kept for three hours to get homogeneous solution. Next, the sample was cooled at a rate of 3 °C/h to 500 °C followed by centrifugation to separate the crystals from flux [12]. Needlelike single crystals were successfully extracted. The phase purity and crystal structure of the as-grown single crystals were determined by powder x-ray diffraction (XRD) technique using Cu-K_α radiation in a PANalytical X′Pert PRO diffractometer. Energy dispersive x-ray spectroscopy (EDS) measurement was performed in a JEOL JSM-6010LA scanning electron microscope to confirm the composition and the homogeneity of the single crystals. Transport measurements were done in a physical property measurement system (PPMS, Quantum Design) via standard four-probe method. Magnetization and heat capacity measurements were also performed in PPMS using the vibrating sample magnetometer and relaxation method, respectively. The band structure computations have been performed based on density functional theory using the projector augmented wave (PAW) method as implemented

*Corresponding author: zakir@iitk.ac.in

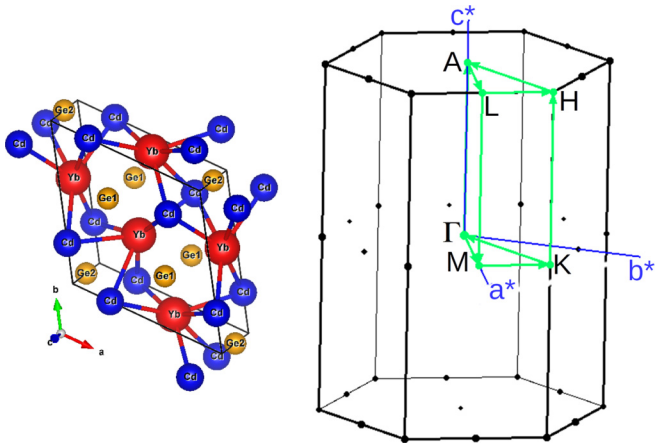

FIG. 1. The crystal structure and Brillouin zone of YbCdGe.

in Vienna *ab initio* simulation package (VASP) [13–21]. The details are provided in the Supplemental Material [23]. As shown in Fig. 1, YbCdGe crystallizes in a hexagonal structure with space group P-62m (189). Here, three Yb, three Cd, two Ge1, and one Ge2 atoms are located at 3g (x, 0, 1/2), 3f (x, 0, 0), 2c (1/3, 2/3, 0), and 1b (0, 0, 1/2) positions, respectively. The XRD data of the crushed single crystals have been analyzed by Rietveld structural refinement using the FULLPROF software package [22] as shown in Fig. S1(a) (see Supplemental Material [23]). Within our experimental resolution, we have not observed any impurity phase. The refined lattice parameters are $a = b = 7.2816(6)$ Å and $c = 4.4415(3)$ Å. Single crystal XRD measurements have been performed to determine crystal axes as shown in Fig. S1(b) (see Supplemental Material [23]). The EDS results (Fig. S2 in Supplemental Material [23]) confirm almost perfect stoichiometry of the grown crystals. The temperature dependent zero-field-cooled (ZFC) magnetic susceptibility of YbCdGe is shown in Fig. 2(a). The calculated value of effective magnetic moment of Yb from Curie-Weiss fitting is $\mu_{\text{eff}} = 3.69\ \mu_B$, which is less than that of $Yb^{3+}(4.54\mu_B)$ state but higher than that of $Yb^{2+}(0\ \mu_B)$ state. This indicates an intermediate valency of Yb in the compound. The valence fluctuating nature has also been revealed by two-level ionic interconfiguration fluctuations (ICF) model fitting of the magnetic susceptibility, which has been discussed in the Supplemental Material [23–31]. In Fig. 2(b), we have plotted the specific heat divided by temperature (C_P/T) of YbCdGe as a function of T in the range 2–30 K. The measured value of C_P/T at 2 K is 41 mJ mol^{-1} K^{-2}, which is smaller than that observed for heavy fermion systems but higher than that of noncorrelated electron systems. Such moderate γ value has been found in several intermediate valence compounds like $YbAl_3$ (γ = 58 mJ mol^{-1} K^{-2}), $YbFe_2Al_{10}$ (γ = 35 mJ mol^{-1} K^{-2}), and $YbFe_4Sb_{12}$ (γ = 140 mJ mol^{-1} K^{-2}) due to the presence of significant electron correlation [32–34]. In rare-earth based valence fluctuating compounds, the interaction between 4-f electrons and conduction electrons enhance the effective mass which leads to increase the γ value of these compounds. As shown in Fig. 3(a), the electrical resistivity (ρ) of YbCdGe decreases almost linearly as temperature decreases from 300 to 70 K. However, below 25 K, $\rho \propto T^3$ behavior is found down to 10 K and then resistivity saturates with a residual resistivity of 21 $\mu\Omega$-cm [inset of Fig. 3(a)]. A deviation from pure electron-electron (n = 2) and electron-phonon (n = 5) interaction is also observed in other TSMs such as ZrSiS (n = 3) [35], $MoAs_2$ (n = 3) [36], LaBi (n = 3) [37], and LaSb (n = 4) [38]. Under the application of magnetic field, we have observed metal-semiconductor-like crossover and resistivity plateau at low temperature, which are generic features of TSMs [35,38–45]. These phenomena can be explained by considering thermally activated energy gap opening model [38] or Kohler's scaling analysis [45]. In Fig. 3(b), the first

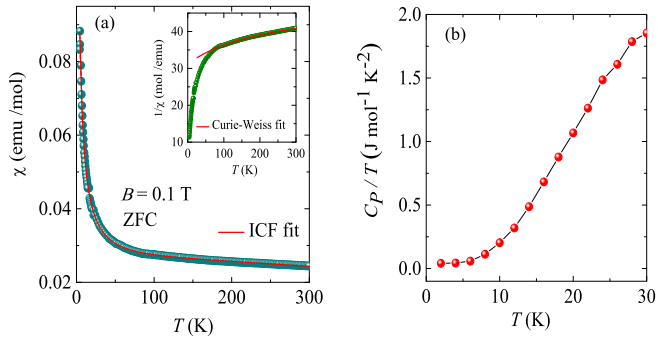

FIG. 2. (a) The experimental data have been fitted with a two-level ionic interconfiguration fluctuations (ICF) model. The Curie-Weiss fitting is shown in the inset. (b) Temperature dependence of the specific heat.

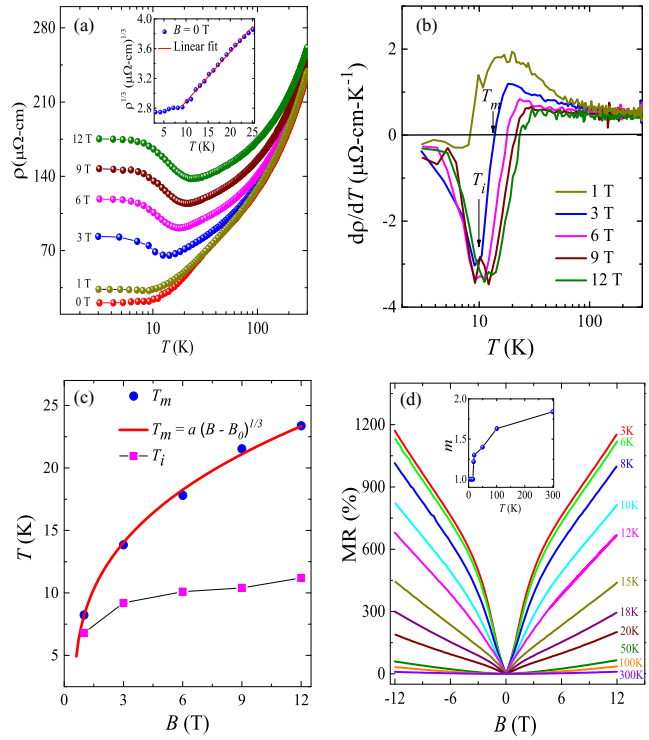

FIG. 3. (a) Temperature dependent resistivity for $0 \leqslant B \leqslant 12$ T, (b) First derivative of resistivity as a function of temperature. (c) T_m and T_i as a function of magnetic field. (d) Magnetoresistance as a function of magnetic field from 3 K to 300 K ($B \perp I$ and $I \parallel c$ axis).

derivative of resistivity ($d\rho/dT$) is shown as a function of temperature. From this figure, two different characteristic temperatures can be clearly identified, T_m and T_i. T_m is the metal-semiconductor-like crossover temperature, where the $d\rho/dT$ curve changes sign. On the other hand, the minimum in $d\rho/dT$ represents T_i, which is the point of inflection in resistivity. The resistivity plateau starts to appear slightly below T_i. T_m increases with increasing magnetic field and follows the relation $T_m \propto (B - B_0)^{1/3}$ as shown in Fig. 3(c), whereas T_i is almost independent of magnetic field. In Fig. 3(d), the MR of YbCdGe is plotted as a function of magnetic field at different temperatures. The compound exhibits extremely large, nonsaturating MR of 1.14×10^3% at 3 K and 12 T, which is about the same order of its sister compound CaCdGe [12] and comparable to several other TSMs [36,46–49]. We have observed that the MR varies over a wide range, depending on the quality of the crystals. Here, we have presented the results for a high quality crystal as a representative and the data are reproduced by other high quality crystals. The MR decreases with increasing temperature and becomes ∼10% at 300 K and 12 T. Interestingly, the MR shows linear magnetic field dependence in the low temperature region (3 K$\leqslant T \leqslant$15 K) and almost quadratic field dependence at room temperature. To determine how the nature of the MR curves change, we have fitted the experimental data with the expression $\mathrm{MR} = qB^m$. The temperature dependence of the exponent m is shown in the inset of Fig. 3(d). According to Kohler's rule $\mathrm{MR} = \alpha(B/\rho_0)^m$, the MR data is plotted as a function of B/ρ_0 as shown in Fig. S3 (Supplemental Material [23]) but the MR data at different temperatures do not merge to a single curve which indicates the MR data violate Kohler's scaling. Violation of Kohler's scaling has been also observed in several noncompensated topological semimetal [35,50–52]. Another prominent feature of the MR is the cusp in the low field region (from −1.5 T to 1.5 T) at 3 K. With increasing temperature, this behavior becomes very weak above 10 K. Such magnetic field dependence of MR is reminiscent of WAL effect and is commonly observed in TIs due to the nontrivial conducting surface states [53,54]. Moreover, WAL effect has also been observed in half-Heusler TSMs such as LuPdBi and LuPtSb single crystals [55,56] and thin films of Dirac semimetal Cd_3As_2 [57]. To have further insight, we have analyzed the behavior of resistivity in low-field region, as shown in Fig. 4(a). The field dependent normalized magnetoconductivity [σ (normalized)$= \sigma(B)/\sigma(0)$] is calculated in the temperature range 3–10 K, where $\sigma(B)$ and $\sigma(0)$ are the conductivity in the presence and absence of magnetic field, respectively. WAL is described by the Hikami-Larkin-Nagaoka (HLN) formula [58],

$$\sigma = \frac{\alpha e^2}{2\pi^2\hbar}\left[\Psi\left(\frac{1}{2}+\frac{\hbar}{4el_\phi^2 B}\right) - ln\left(\frac{\hbar}{4el_\phi^2 B}\right)\right], \qquad (1)$$

where Ψ is the digamma function, l_ϕ is the phase coherence length, and $\alpha = -1/2$ per conduction channel. Thus, the number of conducting channels can be estimated from the value of α. We have fitted the magnetoconductivity data with HLN formula at different temperatures. In Fig. 4(b), one such fitting at 3 K in the magnetic field range ±1.5 T is shown as a representative. We have observed that the experimental

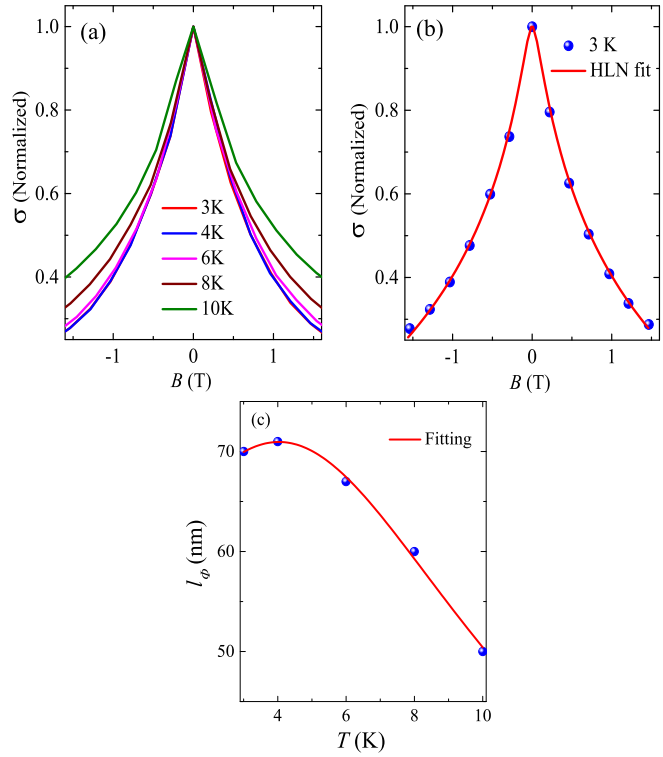

FIG. 4. (a) Magnetoconductivity as a function of magnetic field. (b) HLN fit from −1.5 T to 1.5 T for 3 K data. (c) Phase coherence length fitting using Eq. (2). ($B \perp I$ and $I \parallel c$ axis).

results are in excellent agreement with the HLN formula within this temperature range (3–10 K). From the fitting, the value of α is estimated to be on the order of -10^5, which is five orders larger than that for two-dimensional systems. Such large α value is also observed in three-dimensional topological materials due to the dominance of conducting bulk channels [55,56,59]. The value of α remains constant for all temperatures up to 10 K, which indicates that the number of conducting channel is independent of temperature. In Fig. 4(c), the temperature dependence of l_ϕ is shown, which follows the relation

$$\frac{1}{l_\phi^2(T)} = \frac{1}{l_\phi^2(0)} + A_{ee}T + A_{ep}T^2. \qquad (2)$$

Here, $l_\phi(0)$ is the zero-temperature phase coherence length, and $A_{ee}T$ and $A_{ep}T^2$ represent the electron-electron and electron-phonon interaction, respectively. To further clarify the origin of the WAL, MR measurements are performed by varying the magnetic field direction with respect to the current [Fig. 5(a)]. In Fig. 5(b), the variation of magnetoconductivity, obtained at 3 K, is shown as a function of the normal component of the applied magnetic field, i.e., $B\sin\theta$, where θ is the angle between magnetic field and current. If WAL is originated only from topological surface states then the magnetoconductivity curves for different $B\sin\theta$ should scale to a universal curve as has been observed in low carrier density topological systems [54,59]. In YbCdGe, however, the magnetoconductivity curves at different angles neither merge with magnetic field nor with normal component of magnetic

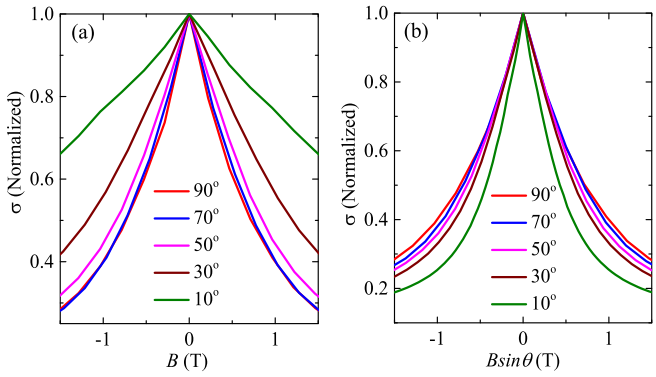

FIG. 5. Magnetoconductivity as a function of (a) B and (b) $B\sin\theta$ at 3 K from -1.5 T to 1.5 T. ($I \parallel c$ axis and θ is the angle between I and B).

field, indicating the presence and superposition of both 3D bulk and 2D surface states [59].

Hall resistivity (ρ_{xy}) data is taken under both positive and negative magnetic field and we have subtracted the MR contribution by using the expression $\rho_{xy} = [\rho_{xy}(B) - \rho_{xy}(-B)]/2$. Figure 6 shows that ρ_{xy} is positive at 2 K, which suggests that hole-type carriers dominate charge conduction. ρ_{xy} is linear in the low-field region up to 5 T, above which an upward curvature starts to appear. Similar concave-upward curvature in the magnetic field dependence of ρ_{xy} has also been reported in an isostructural compound CaAgAs due to the existence of thermally excited electrons occupying the conduction band above the spin-orbit gap [60]. From the linear fit, the hole carrier concentration (n) and the Hall mobility (μ) have been calculated by using the relation $n = 1/(eR_H)$ and $\mu = R_H/\rho_{(B=0)}$, where R_H is the slope of the $\rho_{xy}(B)$ curve. The estimated values of n and μ are $\sim 3.37 \times 10^{20}$ cm^{-3} and ~ 253 cm^2 V^{-1} s^{-1}, respectively. This carrier mobility is less than those reported for noncorrelated TSMs but comparable to strongly correlated topological material such as SmB_6 (~ 133 cm^2 V^{-1} s^{-1}) [61]. The band structures of YbCdGe are shown in Figs. 7(a), 7(b) and 7(c), which have been calculated in the absence and presence of spin-orbit coupling (SOC). Three bands, marked in pink, blue, and red, cross the Fermi level (E_F) [Fig. 7(a)].

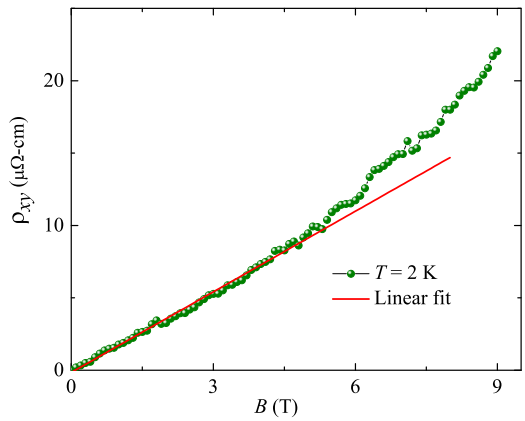

FIG. 6. Hall resistivity as a function of magnetic field at 2 K, where $B \perp I$ and $I \parallel c$ axis.

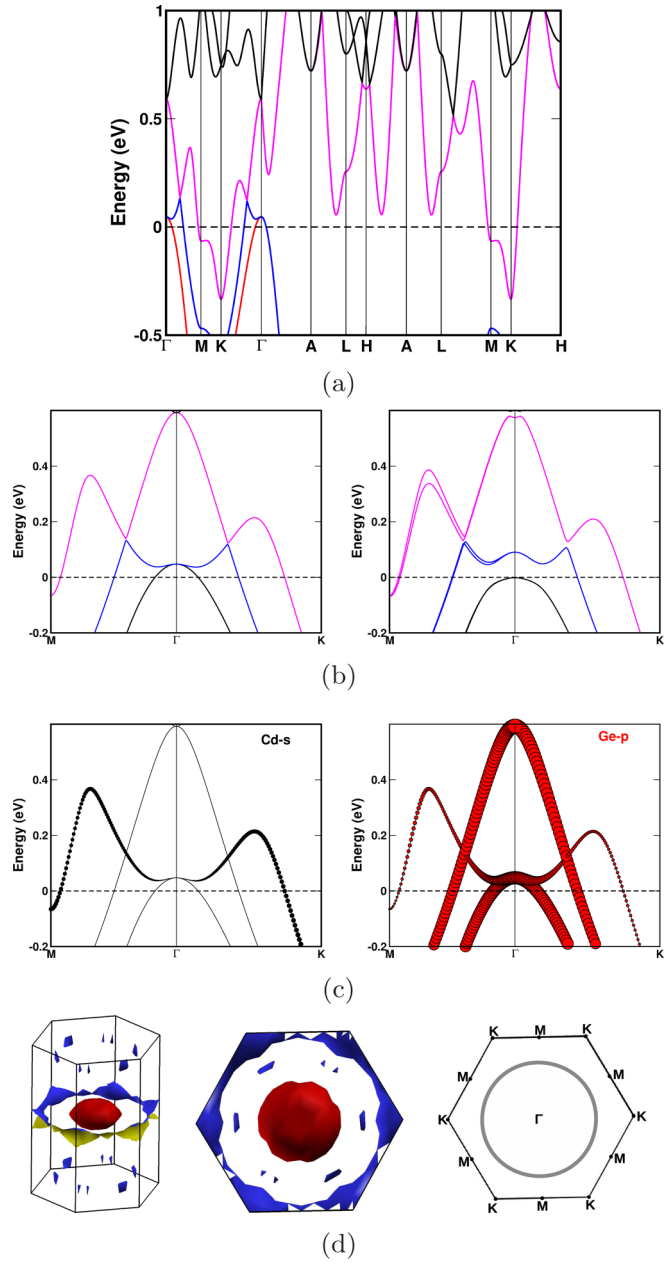

FIG. 7. (a) The band structure of YbCdGe without SOC. (b) Band structure along M-Γ-K path without SOC (left panel) and with SOC (right panel). (c) Projected bands along M-Γ-K path without SOC (left panel) and with SOC (right panel). (d) The Fermi surface in side view (left panel), top view (middle panel), and the schematic nodal-line associated with it (right panel).

The band structure of YbCdGe resembles the band structure of nodal-line semimetal CaCdGe [12]. Hence, it is expected that YbCdGe is also a possible nodal-line semimetal. The noncentrosymmetric compounds CaAgX (X = As, P), which crystallize in the P-62m space group are recently proposed to be nodal-line semimetals [62]. In these semimetals, two nontrivial bulk bands touch along a line, while no trivial bands exist at the E_F. Only nontrivial Fermi pockets, linked by the topological nodal line, are present at the Fermi level in CaAgX [62]. Recently, Emmanouilidou *et al.* [12] have studied the

nodal-line behavior of CaCdGe and concluded that in addition to the nontrivial band carrying the nodal-line feature as proposed in CaAgX, an extra trivial band also crosses the Fermi energy in CaCdGe. Due to this trivial band in CaCdGe, it has a more complicated fermiology with irrelevant Fermi pockets. Coming to YbCdGe, the contribution to these three bands, which cross the E_F, comes mainly from Ge-p and Cd-s orbitals and partly from the Yb-d orbital. We can observe few highly linearly dispersed Dirac points along Γ-M and Γ-K paths within the range of 0.1–0.14 eV together with linear dispersions along L-M, L-H, and H-A in high energy ranges. The same bands are found to split upon the inclusion of SOC which is shown in Fig. 7(b). As we mentioned earlier, two Dirac-like points along Γ-K and Γ-M, which are lying almost in the same energy level, indicate the presence of nodal line in this compound. The band structure of YbCdGe along M-Γ-K without and with SOC is shown in Fig. 7(b). To check the nontrivial nature of the bands, we have plotted projected bands of YbCdGe along the M-Γ-K path as shown in Fig. 7(c). The constituent bands, which form the Dirac-like points, are derived from two different band characters near the Γ point, the Cd-s character lying below Ge-p character with band inversion similar to that of CaAgAs [12]. The plot clearly shows the band crossings between Cd-s and Ge-p orbitals along Γ-M and Γ-K paths and confirms the nontrivial nature of these bands. Without SOC, the two nontrivial bands touch along Γ-M and Γ-K, which lead to a constant energy loop above E_F forming a nodal line similar to CaCdGe as shown in Fig. 7(b). When SOC is included, the gap opens up at two touching points and the corresponding complicated Fermi surface is shown in Fig. 7(d) with side, top views, and the schematic of the nodal loop associated with it.

We note that the carrier density in topological nodal-line semimetals is generally higher than those for Dirac/Weyl semimetals because of Dirac band crossing along a line or loop [63]. From Hall measurements, the estimated carrier density for YbCdGe is $\sim 10^{20}$ cm^{-3}, which is about two orders of magnitude higher than that reported for Dirac/Weyl semimetals [46,64–67] but comparable to isostructural nodal-line semimetals CaCdGe and CaAgAs ($\sim 10^{20}$ cm^{-3}) [12] and another family of nodal-line semimetals ZrSiX (X = S,Se,Te) [63,68]. In this way, we notice a connection between YbCdGe and other nodal-line semimetals through carrier density.

In conclusion, ternary rare-earth based compound YbCdGe shows strongly correlated phenomenon (valence fluctuation) as revealed by magnetic susceptibility and heat capacity measurements. Magnetotransport data indicate that this compound behaves like a topological semimetal. Metal-semiconductor-like crossover and resistivity plateau are observed under the application of magnetic field. At 3 K and 12 T, YbCdGe shows an extremely large, nonsaturating MR $\sim 1.14 \times 10^3$%. A cusp-like magnetoconductivity at low magnetic field suggests the presence of weak antilocalization effect in this system, which originates from the superposition of topologically nontrivial surface state and 3D bulk states. Positive Hall resistance indicates that holes are the dominant charge carriers. Band structure calculations reveal that YbCdGe is a nodal-line semimetal with complicated Fermi surface and warrant further confirmation from angle resolved photoemission spectroscopy measurement.

We gratefully acknowledge financial support from IIT Kanpur, SINP Calcutta, and IIT Hyderabad.

[1] N. Xu, X. Shi, P. K. Biswas, C. E. Matt, R. S. Dhaka, Y. Huang, N. C. Plumb, M. Radović, J. H. Dil, E. Pomjakushina, K. Conder, A. Amato, Z. Salman, D. M. Paul, J. Mesot, H. Ding, and M. Shi, Phys. Rev. B **88**, 121102 (2013).
[2] M. Neupane, N. Alidoust, S.-Y. Xu, T. Kondo, Y. Ishida, D. J. Kim, C. Liu, I. Belopolski, Y. J. Jo, T.-R. Chang, H.-T. Jeng, T. Durakiewicz, L. Balicas, H. Lin, A. Bansil, S. Shin, Z. Fisk, and M. Z. Hasan, Nat. Commun. **4**, 2991 (2013).
[3] C. Y. Guo, F. Wu, Z. Z. Wu, M. Smidman, C. Cao, A. Bostwick, C. Jozwiak, E. Rotenberg, Y. Liu, F. Steglich, and H. Q. Yuan, Nat. Commun. **9**, 4622 (2018).
[4] T. Takimoto, J. Phys. Soc. Jpn. **80**, 123710 (2011).
[5] M. Xia, J. Jiang, Z. R. Ye, Y. H. Wang, Y. Zhang, S. D. Chen, X. H. Niu, D. F. Xu, F. Chen, X. H. Chen, B. P. Xie, T. Zhang, and D. L. Feng, Sci. Rep. **4**, 5999 (2014).
[6] H. Weng, J. Zhao, Z. Wang, Z. Fang, and X. Dai, Phys. Rev. Lett. **112**, 016403 (2014).
[7] Y. Xu, C. Yue, H. Weng, and X. Dai, Phys. Rev. X **7**, 011027 (2017).
[8] A. N. Rudenko, E. A. Stepanov, A. I. Lichtenstein, and M. I. Katsnelson, Phys. Rev. Lett. **120**, 216401 (2018).
[9] S. Pezzini, M. R. van Delft, L. M. Schoop, B. V. Lotsch, A. Carrington, M. I. Katsnelson, N.. E. Hussey, and S. Wiedmann, Nat. Phys. **14**, 178 (2017).
[10] P. Gegenwart, J. Custers, C. Geibel, K. Neumaier, T. Tayama, K. Tenya, O. Trovarelli, and F. Steglich, Phys. Rev. Lett. **89**, 056402 (2002).
[11] J. Paglione, M. A. Tanatar, D. G. Hawthorn, E. Boaknin, R. W. Hill, F. Ronning, M. Sutherland, L. Taillefer, C. Petrovic, and P. C. Canfield, Phys. Rev. Lett. **91**, 246405 (2003).
[12] E. Emmanouilidou, B. Shen, X. Deng, T.-R. Chang, A. Shi, G. Kotliar, S.-Y. Xu, and N. Ni, Phys. Rev. B **95**, 245113 (2017).
[13] G. Kresse and J. Furthmüller, Phys. Rev. B **54**, 11169 (1996).
[14] P. E. Blöchl, Phys. Rev. B **50**, 17953 (1994).
[15] G. Kresse and J. Furthmüller, Comput. Mater. Sci. **6**, 15 (1996).
[16] G. Kresse and J. Hafner, Phys. Rev. B **47**, 558 (1993).
[17] G. Kresse and D. Joubert, Phys. Rev. B **59**, 1758 (1999).
[18] J. P. Perdew, K. Burke, and M. Ernzerhof, Phys. Rev. Lett. **77**, 3865 (1996).
[19] S. L. Dudarev, G. A. Botton, S. Y. Savrasov, C. J. Humphreys, and A. P. Sutton, Phys. Rev. B **57**, 1505 (1998).
[20] H. J. Monkhorst and J. D. Pack, Phys. Rev. B **13**, 5188 (1976).
[21] C. Elsässer, M. Fähnle, C. T. Chan, and K. M. Ho, Phys. Rev. B **49**, 13975 (1994).
[22] J. Rodríguez-Carvajal, Physica B: Condensed Matter **192**, 55 (1993).

[23] See Supplemental Material at http://link.aps.org/supplemental/10.1103/PhysRevB.99.241102 for XRD pattern, EDS data, ICF model fitting expression, and Kohler's scaling.

[24] S. Layek, V. Anand, and Z. Hossain, J. Magn. Magn. Mater. **321**, 3447 (2009).

[25] Y. Matsumoto, K. Kuga, T. Tomita, Y. Karaki, and S. Nakatsuji, Phys. Rev. B **84**, 125126 (2011).

[26] L. L. Hirst, Phys. Condens. Mater. **11**, 255 (1970).

[27] B. C. Sales and D. K. Wohlleben, Phys. Rev. Lett. **35**, 1240 (1975).

[28] W. Franz, F. Steglich, W. Zell, D. Wohlleben, and F. Pobell, Phys. Rev. Lett. **45**, 64 (1980).

[29] D. T. Adroja, S. K. Malik, B. D. Padalia, S. N. Bhatia, R. Walia, and R. Vijayaraghavan, Phys. Rev. B **42**, 2700 (1990).

[30] A. Kowalczyk, M. Falkowski, and T. Toliski, J. Appl. Phys. **107**, 123917 (2010).

[31] D. Kaczorowski, A. V. Gribanov, P. Rogl, and S. F. Dunaev, J. Alloys Compd. **685**, 957 (2016).

[32] T. Ebihara, S. Uji, C. Terakura, T. Terashima, E. Yamamoto, Y. Haga, Y. Inada, and Y. Onuki, Physica B: Condensed Matter **281-282**, 754 (2000).

[33] J. L. Lv, R. Y. Chen, H. P. Wang, J. L. Luo, and N. L. Wang, Phys. Rev. B **95**, 235132 (2017).

[34] N. R. Dilley, E. J. Freeman, E. D. Bauer, and M. B. Maple, Phys. Rev. B **58**, 6287 (1998).

[35] R. Singha, A. K. Pariari, B. Satpati, and P. Mandal, Proc. Natl. Acad. Sci. USA **114**, 2468 (2017).

[36] R. Singha, A. Pariari, G. K. Gupta, T. Das, and P. Mandal, Phys. Rev. B **97**, 155120 (2018).

[37] S. Sun, Q. Wang, P.-J. Guo, K. Liu, and H. Lei, New J. Phys. **18**, 082002 (2016).

[38] F. F. Tafti, Q. D. Gibson, S. K. Kushwaha, N. Haldolaarachchige, and R. J. Cava, Nat. Phys. **12**, 272 (2015).

[39] Y.-Y. Wang, Q.-H. Yu, P.-J. Guo, K. Liu, and T.-L. Xia, Phys. Rev. B **94**, 041103(R) (2016).

[40] Y. Li, L. Li, J. Wang, T. Wang, X. Xu, C. Xi, C. Cao, and J. Dai, Phys. Rev. B **94**, 121115 (2016).

[41] L.-K. Zeng, R. Lou, D.-S. Wu, Q. N. Xu, P.-J. Guo, L.-Y. Kong, Y.-G. Zhong, J.-Z. Ma, B.-B. Fu, P. Richard, P. Wang, G. T. Liu, L. Lu, Y.-B. Huang, C. Fang, S.-S. Sun, Q. Wang, L. Wang, Y.-G. Shi, H. M. Weng, H.-C. Lei, K. Liu, S.-C. Wang, T. Qian, J.-L. Luo, and H. Ding, Phys. Rev. Lett. **117**, 127204 (2016).

[42] W. Gao, N. Hao, F.-W. Zheng, W. Ning, M. Wu, X. Zhu, G. Zheng, J. Zhang, J. Lu, H. Zhang, C. Xi, J. Yang, H. Du, P. Zhang, Y. Zhang, and M. Tian, Phys. Rev. Lett. **118**, 256601 (2017).

[43] M. N. Ali, L. M. Schoop, C. Garg, J. M. Lippmann, E. Lara, B. Lotsch, and S. S. P. Parkin, Sci. Adv. **2** e1601742 (2016).

[44] R. Singha, A. Pariari, B. Satpati, and P. Mandal, Phys. Rev. B **96**, 245138 (2017).

[45] Y. L. Wang, L. R. Thoutam, Z. L. Xiao, J. Hu, S. Das, Z. Q. Mao, J. Wei, R. Divan, A. Luican-Mayer, G. W. Crabtree, and W. K. Kwok, Phys. Rev. B **92**, 180402 (2015).

[46] A. Narayanan, M. D. Watson, S. F. Blake, N. Bruyant, L. Drigo, Y. L. Chen, D. Prabhakaran, B. Yan, C. Felser, T. Kong, P. C. Canfield, and A. I. Coldea, Phys. Rev. Lett. **114**, 117201 (2015).

[47] N. Wakeham, E. D. Bauer, M. Neupane, and F. Ronning, Phys. Rev. B **93**, 205152 (2016).

[48] M. Novak, S. Sasaki, K. Segawa, and Y. Ando, Phys. Rev. B **91**, 041203(R) (2015).

[49] O. Pavlosiuk, P. Swatek, and P. Wisniewski, Sci. Rep. **6**, 38691 (2016).

[50] A. Wang, D. Graf, Y. Liu, Q. Du, J. Zheng, H. Lei, and C. Petrovic, Phys. Rev. B **96**, 121107 (2017).

[51] J. Wang, L. Li, W. You, T. Wang, C. Cao, J. Dai, and Y. Li, Sci. Rep. **7**, 15669 (2017).

[52] R. H. McKenzie, J. S. Qualls, S. Y. Han, and J. S. Brooks, Phys. Rev. B **57**, 11854 (1998).

[53] J. Chen, H. J. Qin, F. Yang, J. Liu, T. Guan, F. M. Qu, G. H. Zhang, J. R. Shi, X. C. Xie, C. L. Yang, K. H. Wu, Y. Q. Li, and L. Lu, Phys. Rev. Lett. **105**, 176602 (2010).

[54] H.-T. He, G. Wang, T. Zhang, I.-K. Sou, G. K. L. Wong, J.-N. Wang, H.-Z. Lu, S.-Q. Shen, and F.-C. Zhang, Phys. Rev. Lett. **106**, 166805 (2011).

[55] G. Xu, W. Wang, X. Zhang, Y. Du, E. Liu, S. Wang, G. Wu, Z. Liu, and X. X. Zhang, Sci. Rep. **4**, 5709 (2014).

[56] Z. Hou, Y. Wang, G. Xu, X. Zhang, E. Liu, W. Wang, Z. Liu, X. Xi, W. Wang, and G. Wu, Appl. Phys. Lett. **106**, 102102 (2015).

[57] B. Zhao, P. Cheng, H. Pan, S. Zhang, B. Wang, G. Wang, F. Xiu, and F. Song, Sci. Rep. **6**, 22377 (2016).

[58] S. Hikami, A. I. Larkin, and Y. Nagaoka, Prog. Theor. Phys. **63**, 707 (1980).

[59] K. Shrestha, M. Chou, D. Graf, H. D. Yang, B. Lorenz, and C. W. Chu, Phys. Rev. B **95**, 195113 (2017).

[60] Y. Okamoto, T. Inohara, A. Yamakage, Y. Yamakawa, and K. Takenaka, J. Phys. Soc. Jpn. **85**, 123701 (2016).

[61] P. Syers, D. Kim, M. S. Fuhrer, and J. Paglione, Phys. Rev. Lett. **114**, 096601 (2015).

[62] A. Yamakage, Y. Yamakawa, Y. Tanaka, and Y. Okamoto, J. Phys. Soc. Jpn. **85**, 013708 (2016).

[63] J. Hu, Z. Tang, J. Liu, X. Liu, Y. Zhu, D. Graf, K. Myhro, S. Tran, C. N. Lau, J. Wei, and Z. Mao, Phys. Rev. Lett. **117**, 016602 (2016).

[64] T. Liang, Q. Gibson, M. N. Ali, M. Liu, R. J. Cava, and N. P. Ong, Nat. Mater. **14**, 280 (2014).

[65] Y. Zhao, H. Liu, C. Zhang, H. Wang, J. Wang, Z. Lin, Y. Xing, H. Lu, J. Liu, Y. Wang, S. M. Brombosz, Z. Xiao, S. Jia, X. C. Xie, and J. Wang, Phys. Rev. X **5**, 031037 (2015).

[66] L. P. He, X. C. Hong, J. K. Dong, J. Pan, Z. Zhang, J. Zhang, and S. Y. Li, Phys. Rev. Lett. **113**, 246402 (2014).

[67] B. Q. Lv, H. M. Weng, B. B. Fu, X. P. Wang, H. Miao, J. Ma, P. Richard, X. C. Huang, L. X. Zhao, G. F. Chen, Z. Fang, X. Dai, T. Qian, and H. Ding, Phys. Rev. X **5**, 031013 (2015).

[68] J. Hu, Z. Tang, J. Liu, Y. Zhu, J. Wei, and Z. Mao, Phys. Rev. B **96**, 045127 (2017).